PNAS RESEARCH ARTICLE | BIOPHYSICS AND COMPUTATIONAL BIOLOGY

Calcium-activated chloride channel TMEM16A opens via pi-helical transition in transmembrane segment 4

Andrei Y. Kostritskii[a,1], Yulia Kostritskaia[b], Natalia Dmitrieva[a], Tobias Stauber[b], and Jan-Philipp Machtens[a,c,1]

Affiliations are included on p. 10.

Edited by Alessio Accardi, Cornell–Weill Cornell Medical College, New York, NY; received October 22, 2024; accepted March 27, 2025, by Editorial Board Member Francisco Bezanilla

TMEM16A is a Ca^{2+}-activated Cl^- channel that has crucial roles in various physiological and pathological processes. However, the structure of the open state of the channel and the mechanism of Ca^{2+}-induced pore opening have remained elusive. Using extensive molecular dynamics simulations, protein structure prediction, and patch-clamp electrophysiology, we demonstrate that TMEM16A opens a hydrated Cl^--conductive pore via a pi-helical transition in transmembrane segment 4 (TM4). We also describe a coupling mechanism that links pi-helical transition and pore opening to the Ca^{2+}-induced conformational changes in TMEM16A. Furthermore, we designed a pi-helix-stabilizing mutation (I551P) that facilitates TMEM16A activation, revealing atomistic details of the ion-conduction mechanism. Finally, AlphaFold2 structure predictions revealed the importance of the pi helix in TM4 to structure–function relations in TMEM16 and the related OSCA/TMEM63 family, further highlighting the relevance of dynamic pi helices for gating in various ion channels.

TMEM16A | chloride channel | electrophysiology | gating | molecular dynamics

TMEM16A (also known as ANO1) is a Ca^{2+}-activated Cl^- channel (1–3) that is expressed in various tissues including epithelium, smooth muscles, and neurons (4, 5). Accordingly, TMEM16A has roles in multiple physiological processes such as epithelial Cl^- secretion, smooth muscle contraction, and nociception (4, 5). In particular, activation of TMEM16A in the airway epithelium is considered a potential therapeutic strategy to alleviate deficient epithelial fluid secretion in patients with cystic fibrosis (CF) (6). TMEM16A malfunction in smooth muscle may be linked to hypertension (4, 5), whereas overexpression of the channel has been associated with the pathogenesis of several types of cancer (7). Although TMEM16A is a promising pharmacological target for the treatment of CF, hypertension, and cancer, its broad expression currently limits a pharmacological application (6, 8). While adverse off-target effects can be alleviated by state-specific drugs (8), the development of such drugs requires a comprehensive and detailed mechanistic understanding of TMEM16A activation and ion conduction.

TMEM16A functions as a homodimer (9–11) of two independently activated protomers (12, 13). The overall dimeric architecture of TMEM16A (Fig. 1*A*) revealed by cryogenic electron microscopy (cryo-EM) studies (14–16) is similar to that of the homologous TMEM16 lipid scramblase from *Nectria haematococca* (nhTMEM16), whose X-ray structure (17) provided the first structural insights into the TMEM16 family. Each protomer of TMEM16A contains 10 transmembrane segments (18) (TMs) and forms an individual ion-conducting pore lined by TMs 3 to 7 (Fig. 1*B*). Binding of Ca^{2+} to the main site (19) formed by TMs 6 to 8 induces a prominent structural rearrangement in TM6 that eventually leads to channel opening (15, 20). Additionally, channel activation is allosterically modulated by an auxiliary Ca^{2+}-binding site that is formed at the dimer interface (21). Furthermore, gating of TMEM16A is regulated by voltage (22), pH (23), permeating anions (24), and lipids (25) including phosphatidylinositol-(4,5)-bisphosphate (25–31).

A recent comprehensive noise-analysis study demonstrated that at saturating Ca^{2+} concentration, the rather complex gating mechanism (32) of TMEM16A can be largely reduced to a four-state model in which the final open state of the channel is reached from a preopen Ca^{2+}-bound state (33). However, capturing the channel in the open state has proven challenging (34), so all of the currently existing experimental structures of TMEM16A in the Ca^{2+}-bound state feature a pore that is too narrow for Cl^- permeation (14–16, 34–36). While the open state has so far evaded structural characterization, the

Significance

TMEM16A is an anion channel whose main physiological function is to couple chloride conduction to the level of intracellular Ca^{2+}. Despite physiological importance and high pharmacological potential of TMEM16A, its gating mechanism remains incompletely understood. Here, we combine molecular dynamics simulations, structure predictions, and electrophysiology to demonstrate that the pore opening in TMEM16A relies on a change in the secondary structure in its transmembrane region. The identified alpha-to-pi-helical transition in the transmembrane segment 4 releases the hydrophobic gate allowing for efficient chloride conduction. Furthermore, we demonstrate how Ca^{2+} binding controls the opening transition, thus providing a unified picture of the channel activation. We believe that our findings will help in developing safe state-dependent drugs targeting TMEM16A.

Author contributions: A.Y.K. designed research; A.Y.K. and Y.K. performed research; N.D. and T.S. contributed new reagents/analytic tools; A.Y.K. analyzed data; and A.Y.K. and J.-P.M. wrote the paper with contributions from all authors.

The authors declare no competing interest.

This article is a PNAS Direct Submission. A.A. is a guest editor invited by the Editorial Board.

[1]To whom correspondence may be addressed. Email: a.kostritskii@fz-juelich.de or j.machtens@fz-juelich.de.

This article contains supporting information online at https://www.pnas.org/lookup/suppl/doi:10.1073/pnas.2421900122/-/DCSupplemental.

Published April 29, 2025.

preopen structure of TMEM16A was recently resolved in complex with the open-pore blocker 1PBC (35). Although 1PBC specifically blocks the channel in the open state, the resolved structure exhibits a sealed hydrophobic gate in the center of the ion-impermeable pore (35). Thus, release of the hydrophobic gate was proposed to underlie the transition of TMEM16A into a final ion-conductive state (33–36). However, the mechanism of this last step in channel opening, as well as its coupling to the initial Ca^{2+}-induced conformational changes, remains unclear.

Here, we used extensive atomistic molecular dynamics (MD) simulations and free-energy calculations complemented by protein structure predictions and patch-clamp electrophysiology to study the mechanisms of gating and ion conduction in TMEM16A. We found that TMEM16A releases the hydrophobic gate and opens its pore via an alpha-to-pi-helical transition in the central part of TM4. The resulting open hydrated pore is permeable to Cl^- ions, with a simulated conductance of ~1 pS that matches experimental values characteristic of TMEM16A. By scrutinizing a few dozen individual Cl^--permeation events, we identified key elements of the ion-conduction mechanism in TMEM16A. We could also stabilize the pi-helical conformation of TM4 by the I551P mutation, which facilitated TMEM16A pore opening in both simulations and patch-clamp experiments. Furthermore, AlphaFold2 structure predictions revealed a connection between the structure of the pi-helical region and its potential functional roles in the TMEM16 and related protein families. Finally, we provide a mechanism linking the Ca^{2+}-induced rearrangement of TM6 to pore opening via the pi-helical transition in TM4, thereby integrating our findings into the general mechanism of TMEM16A activation.

Results

Spontaneous Pi-Helical Transition Opens the Cl^--Conductive Pore. We first conducted a series of unbiased atomistic MD simulations of TMEM16A in the preopen state (PDBID: 7ZK3), which was recently resolved by cryo-EM (35) (Fig. 1 *A* and *B*). We observed the spontaneous transition of TM4 from its native alpha-helical conformation to a kinked structure with a pi bulge in the middle (Fig. 1 *C* and *D*). The transition was characterized by loss of the hydrogen bond (H-bond) between the backbone N and O atoms of residues L547 and I551 (Fig. 1*E*) and the simultaneous formation of a H-bond between residues I545 and I550 (Fig. 1*F*). The transition resulted in dilation of the pore (Fig. 1*D*), as indicated by the increased distance between TM4 and TM5 (Fig. 1*G*). Although minor (~2 Å), the dilation was accompanied by a prominent increase in hydration in the central part of the pore (Fig. 1*G*). Notably, the transition was reversible, with TM4 returning to the original alpha state after ~700 ns in the pi state (Fig. 1 *E*–*G*). Rearrangement of the secondary structure also led to rotation of the residues in the central part of TM4 around the helical axis (Fig. 1*D*). As a result, the hydrophobic L547 residue, which points into the pore in the alpha state, was replaced by the hydrophilic N546 (Fig. 1*D*), thereby releasing the hydrophobic gate and increasing hydration of the pore.

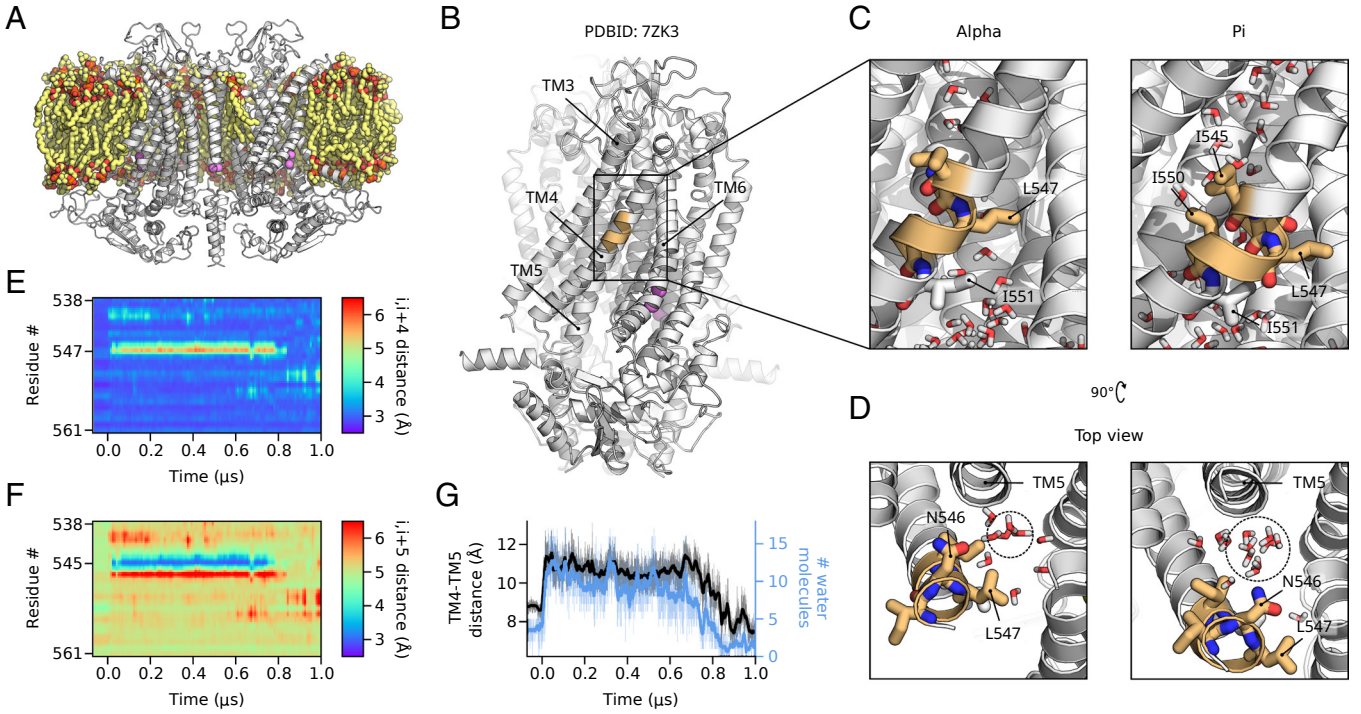

Fig. 1. TMEM16A opens a hydrated pore via pi-helical transition in TM4. (*A*) A snapshot illustrating the simulation system with TMEM16A embedded into a lipid membrane. The protein, lipids, and lipid oxygen atoms are shown in white, yellow, and red, respectively. Water and ions are omitted for clarity. (*B*) Side view of the TMEM16A protomer in the preopen state (PDBID: 7ZK3). (*A* and *B*) Ca^{2+} ions are shown as magenta spheres. (*C* and *D*) Expanded side (*C*) and top (*D*) views of the central part of the pore in the alpha and pi states. Residues involved in the pi-helical transition are shown as sticks. The dashed circle illustrates the increase in pore radius and hydration upon pi-helical transition. (*B*–*D*) The central part of TM4 that undergoes pi-helical transition is highlighted in tan. (*E* and *F*) Time courses of the backbone O–N distance between a TM4 residue *i* and the neighboring $i + 4$ (*E*) or $i + 5$ (*F*) residue, shown as heatmaps. Residue L547, which loses the alpha-helical hydrogen bond (*E*), and I545, which establishes the pi-helical hydrogen bond (*F*), are explicitly indicated. (*G*) Time courses of the distance between TM4 and TM5 (*black*) and number of water molecules in the central part of the pore (*blue*). (*E*–*G*) Negative time corresponds to the equilibration part of the trajectory.

We conducted simulations in five replicates (*SI Appendix*, Table S1), thus collecting data on 10 independent protomers, since TMEM16A protomers function independently within the dimer (12, 13). The pi-helical transition was observed in two of the 10 simulated protomers (*SI Appendix*, Fig. S1). However, in most of the other protomers, the alpha-helical structure of TM4 was disturbed in a region located one helical turn downstream from L547, as indicated by loss of the H-bond between I551 and E555 (*SI Appendix*, Fig. S1*A*). Importantly, the disturbance did not lead to formation of a pi helix in this region (*SI Appendix*, Fig. S1*B*). These data suggest that TM4 can store a portion of bending energy in the region between I551 and E555 without causing opening of the pore. However, when the helical disturbance occurs one helical turn upstream, the bending energy converts the central part of TM4 from the alpha- to a pi-helical conformation, thereby opening the fully hydrated pore.

To rigorously study the properties of the TMEM16A pore in the open state, we conducted a series of simulations in which TM4 was biased toward the pi-helical conformation. For this, we applied a harmonic potential to maintain the distance between the backbone O and N atoms of residues I545 and I550 at 0.3 nm, corresponding to the pi-helical state of the pore. In agreement with the unbiased simulations, the pore remained open and hydrated (Fig. 2*A*). We then estimated the radius of the pore in the alpha and pi states (Fig. 2*B*). Notably, the narrowest part of the hourglass-shaped pore coincides with the TM4 region that undergoes the pi-helical transition. In the alpha state, the narrowest part of the pore is obstructed by L547, making it too narrow to permit permeation of a Cl^- ion, which has a radius of 1.8 Å (Fig. 2 *B* and *C*). The pi-helical transition increases the radius of the narrowest part to ∼4 Å resulting in a pore that is sufficiently wide for Cl^- conduction (Fig. 2 *B* and *C*). Furthermore, increased hydration of the narrowest part of the pore (Fig. 2*D*) caused by the rotation of N546 makes the pore suitable for the conduction of partially hydrated ions.

Finally, we simulated TMEM16A in the pi state in the presence of a transmembrane voltage (±140 mV) and estimated its ion conductance. We observed a total of 19 Cl^- permeation events distributed over 20 protomers, with each simulated for 1 μs. In full agreement with the experimental estimates of ∼1 to 3 pS (12, 20, 33, 37), the calculated mean conductance of the pore in the pi state was ∼1 pS (Fig. 2*E*). We then stabilized TMEM16A in the alpha state, by applying a harmonic potential on the distance between the backbone O and N atoms of residues L547 and I551, and conducted a series of simulations with an applied voltage. Despite the restraint, TM4 underwent the pi-helical transition in regions upstream or downstream the restrained region in three of the 20 simulated protomers (*SI Appendix*, Fig. S2). While this further suggests that TM4 has an inherent tendency to break the native helical structure, these protomers could not be unambiguously assigned to either the alpha or the pi state and, therefore, were discarded from further analysis. Although we did observe a single Cl^- permeation event in one of the simulations of TMEM16A in the alpha state, the pore remained virtually closed with an overall conductance indistinguishable from zero (Fig. 2*E*). Therefore, we conclude that the alpha-helical conformation of TM4 corresponds to the closed state of the pore and that pi-helical transition releases the hydrophobic gate and opens a Cl^--permeable pore with a conductance level of native TMEM16A.

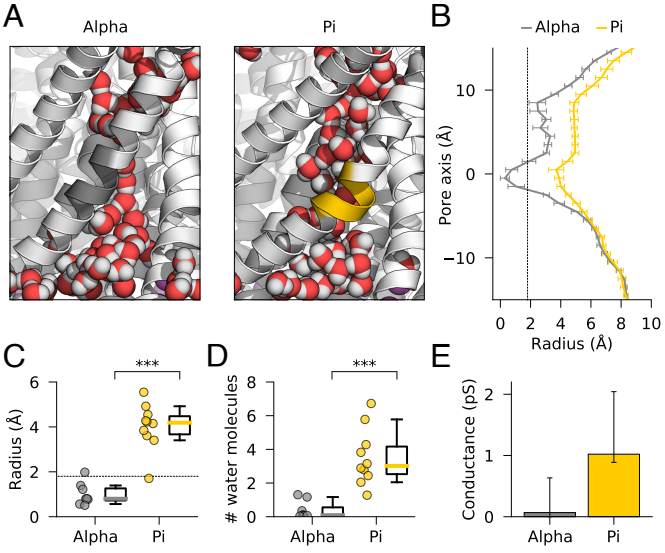

Fig. 2. The pi-helical transition renders the TMEM16A pore Cl^- conductive. (*A*) Snapshots illustrating the increased width and hydration of the pore upon pi-helical transition in transmembrane segment 4. The region of the pi-helical transition is shown in gray in the alpha and gold in the pi state. Water molecules are represented by spheres. (*B*) Radius profile of the TMEM16A pore in the alpha and pi states. Error bars indicate the SEM. (*C* and *D*) Pore radius (*C*) and number of water molecules (*D*) in the narrowest part of the pore in the alpha (n = 8) and pi (n = 10) states. The dashed line (*B* and *C*) indicates the radius of a Cl^- ion. Significance was assessed using a one-tailed t-test, resulting in $P = 4 \times 10^{-5}$ (*C*) and $P = 1 \times 10^{-5}$ (*D*). Each data point corresponds to an individual protomer, with quartiles and the 5th and 95th percentiles indicated by the box and whiskers, respectively. (*E*) Conductance of TMEM16A with the pore restrained in the alpha or pi state. The conductance was calculated from 20 μs of simulations distributed over 20 individual protomers in the pi state, and from 17 μs of simulations distributed over 17 individual protomers in the alpha state. The simulations were conducted with applied transmembrane voltage of ±140 mV. Error bars show the 95% CI, as calculated by bootstrap analysis.

Mechanism of TMEM16A Ion Conduction. By tracking individual Cl^- permeation events through the open pore of TMEM16A, we identified key details of the ion conduction process. The ion permeation pathway is largely shielded from the membrane (Fig. 3*A*), in contrast to TMEM16 lipid scramblases, in which ions are conducted through a proteolipidic pore lined by lipid headgroups (38). Fig. 3*B* shows the three-dimensional density of the permeating Cl^- ions, which clearly indicates two ion localization sites along the ion permeation pathway. These two sites—S0 in the intracellular vestibule and S1 in the extracellular mouth of the pore—are separated by the neck region as seen in the one-dimensional distribution of permeating ions along the pore (Fig. 3*C*). Notably, Cl^- ions lose part of their hydration shell when located in the S0 and S1 sites (Fig. 3*D*). Analysis of the contacts between permeating ions and protein residues (Fig. 3*E*) suggests that the partial loss of hydration stems from tight coordination of the Cl^- ions by residues clustered around the identified ion localization sites (Fig. 3*B*). In particular, the S0 site is formed by residues D554, N646, K588, and K645, with the latter two having the most prominent roles in coordination of the permeating ions (Fig. 3*E*). In the S1 site, Cl^- is mainly stabilized by contacts with basic K603 and R515 (Fig. 3 *B* and *E*), which were previously shown to underlie selectivity of the pore (39). Consistent with these differences in the number of coordinating residues, a Cl^- ion has on average one water molecule fewer in its first hydration shell when located in the S0 than in the S1 site (Fig. 3*D*). Notably, opening of the pore let permeating ions partially restore their hydration shells in the neck region (Fig. 3*D*). Thus, contact with water molecules can compensate for transient interactions of Cl^- with the polar residues (Q637,

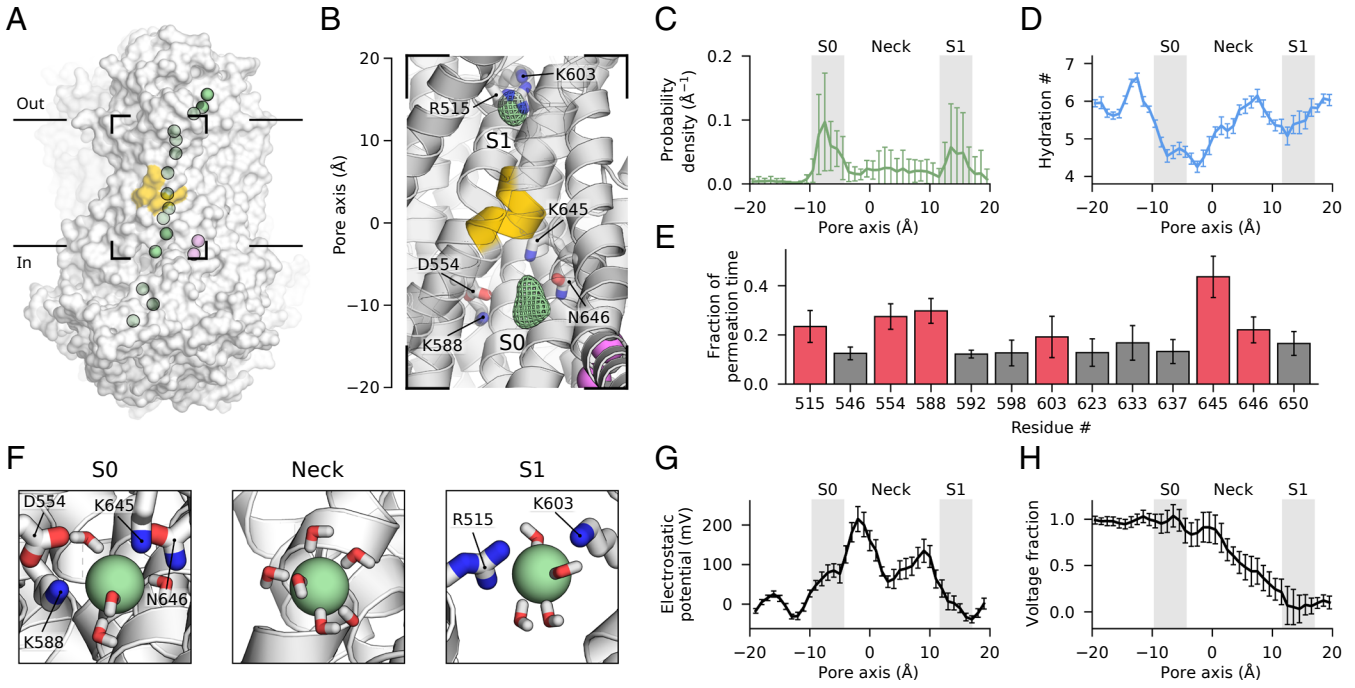

Fig. 3. Mechanism of ion permeation through the open pore of TMEM16A. (*A*) A snapshot of the Cl^- permeation pathway. Green spheres indicate the positions of a Cl^- ion during its permeation through the pore. Bound Ca^{2+} ions are shown as magenta spheres. (*B*) Density of permeating Cl^- ions (shown as a green mesh and contoured at 7σ). Residues that form the identified Cl^- localization sites S0 and S1 are shown as transparent sticks. (*A* and *B*) The pi-helical region of TM4 is highlighted in gold. (*C*) Probability density distribution of permeating Cl^- ions along the pore axis. (*D*) The number of water molecules in the first hydration shell of permeating Cl^- ions depending on their position along the pore axis. (*E*) Fraction of time that permeating Cl^- ions are coordinated by the pore residues, showing only those residues that coordinate ions more than 12% of the time (those coordinating more than 18% of the time are shown in red). (*F*) Milestones of the ion permeation mechanism that is transition between ion localization sites S0 and S1 separated by the neck region. Coordinating residues and water molecules in the first hydration shell of the permeating Cl^- ion are shown as sticks. (*A*–*F*) Data were extracted from simulations with applied transmembrane voltage of ±140 mV. (*G*) Electrostatic-potential profile along the pore axis in the absence of transmembrane voltage. (*H*) Distribution of the voltage fraction sensed by the pore interior along the pore axis at ±140 mV. (*C*–*E*, *G*, and *H*) Error bars indicate the SEM, and ion localization sites S0 and S1 are indicated in gray (*C*, *D*, *G*, and *H*).

S592, and N546) that line the neck region of the pore (Fig. 3*E*). In summary, the ion-conduction process in TMEM16 occurs via the swift transition of a hydrated Cl^- ion between S0 and S1 sites in which the ion sheds part of its hydration shell in exchange for its coordination by protein residues (Fig. 3*F*).

Electrostatics play a profound role in the functioning of TMEM16A (40). To gain atomic-level insight into electrostatics of the open TMEM16A pore, we utilized our recently developed *g_elpot* tool that enables high-resolution quantification of the electrostatic potential based on MD simulations (41). The electrostatic potential is positive along the pore, thus conferring anion selectivity to TMEM16A (Fig. 3*G*). In the neck region, the potential profile features two peaks that are adjacent to the ion localization sites (Fig. 3*G*). Whereas the peaks facilitate the attraction of anions closer to the neck region, the trough between them serves to expel the anion that has just entered the neck. Thus, the double-peak configuration of the electrostatic-potential profile provides a mechanism for swift permeation through the neck region. We also quantified how the pore electrostatics respond to a change in transmembrane voltage. To this end, we calculated the distribution of the voltage fraction that is sensed by the pore interior (see *Materials and Methods* for details), as shown in Fig. 3*H*. Notably, the whole transmembrane voltage is largely focused within a 1-nm-long region coinciding with the neck region of the pore (Fig. 3*H*). Thus, the linear drop in voltage creates a roughly constant electric field that drives the permeation of ions across the membrane. Such a configuration of the electric field is also consistent with the voltage-dependent inhibition of the channel by extracellular blockers (39). In particular, the blockers that bind just below the extracellular Cl^- localization site S0 would already feel a fraction (10 to 20%) of the voltage that drops across the neck region of the pore. At the same time, the ion localization sites lie outside the transmembrane electric field (Fig. 3*H*). In summary, the electrostatics of the pore do not only facilitate the anion selectivity of TMEM16A but also promote the swift transition of permeating ions through the neck, which is flanked by voltage-independent Cl^- localization sites.

I551P Substitution Stabilizes Pi Helix and Facilitates Pore Opening. In unbiased simulations of wild-type (WT) TMEM16A, formation of the pi helix was accompanied by disruption of the alpha-helical H-bond between L547 and I551. Therefore, we predicted that preventing formation of this H-bond by proline substitution could favor formation of the pi helix and, thereby, facilitate opening of the TMEM16A pore. We first introduced the I551P mutation and conducted unbiased MD simulations of the mutant TMEM16A (Fig. 4*A*). Indeed, in the vast majority of I551P simulations, the central part of TM4 adopted the pi-helical conformation (Fig. 4*B*) that was stabilized by the mutation (Fig. 4*A*). Interestingly, another activating mutation I551A also lead to higher propensity of the pore to the pi-helical state compared to WT (*SI Appendix*, Fig. S3), although to a notably lower degree than the I551P mutation. As a result of the pi-helical transition, the narrowest part of the I551P pore was wide enough (*SI Appendix*, Fig. S4*A*) to permit ion permeation with a conductance of ∼1 pS as in the WT channel (Fig. 4*C*). Importantly,

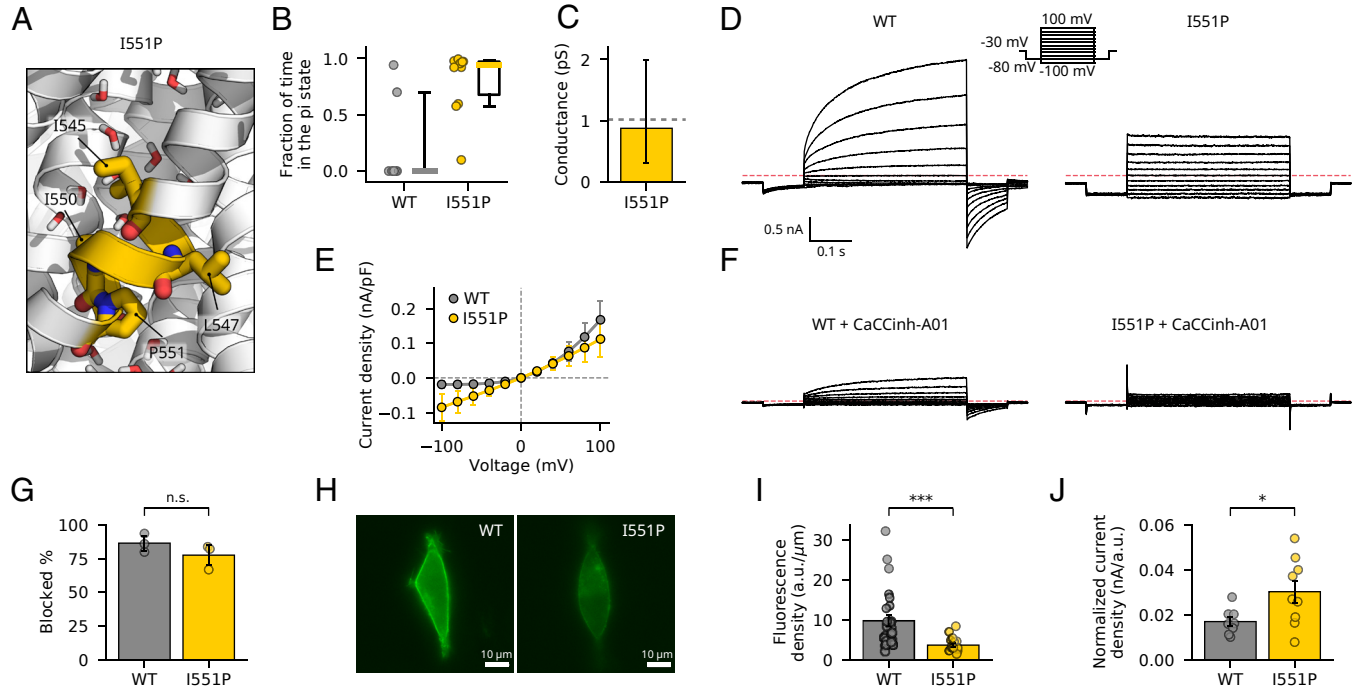

Fig. 4. I551P facilitates pore opening by stabilizing the pi helix in TM4. (*A*) A snapshot showing disruption of the native H-bond between L547 and I551 in the I551P mutant. (*B*) Fraction of time that an individual protomer spends in the pi state in WT and I551P simulations. Each data point corresponds to an individual protomer, with quartiles and the 5th and 95th percentiles indicated by boxes and whiskers, respectively. (*C*) Conductance of I551P TMEM16A as calculated from 28 µs of simulations distributed over 20 individual protomers. The simulations were conducted with applied transmembrane voltage of ±140 mV. The dashed line indicates simulated conductance of WT TMEM16A with the pore restrained in the pi-helical state. Error bars show the 95% CI, as calculated by bootstrap analysis. (*D*) Whole-cell patch-clamp recordings of WT and I551P in the presence of 250 nM free Ca^{2+}. (*E*) Voltage dependence of the WT and I551P currents. (*F*) Whole-cell patch-clamp recordings of WT and I551P in the presence of 250 nM free Ca^{2+} and 20 µM of CaCCinh-A01. (*G*) Percentage of the WT (n = 3) and I551P (n = 3) current at +100 mV that is blocked by 20 µM CaCCinh-A01 ($P = 0.13$). (*H*) Fluorescence imaging of HEK293 cells transfected with the WT or I551P construct. (*I*) Membrane fluorescence density in HEK293 cells expressing WT (n = 25) or I551P (n = 18) channels ($P = 0.0002$). (*J*) Current density at +100 mV normalized by the membrane fluorescence density in cells expressing WT (n = 8) or I551P (n = 9) TMEM16A ($P = 0.016$). Significance was assessed using a one-tailed *t* test. (*E*,*G*,*I*, and *J*) Error bars indicate the SEM.

other biophysical properties of the mutant pore, such as the overall radius profile (*SI Appendix*, Fig. S4*B*), distribution (*SI Appendix*, Fig. S4*C*) and hydration (*SI Appendix*, Fig. S4*D*) of permeating Cl^- ions, and distributions of the electrostatic potential (*SI Appendix*, Fig. S4*E*) and voltage fraction (*SI Appendix*, Fig. S4*F*) along the pore were virtually indistinguishable from those of the WT pore in the open pi-helical state. Thus, the simulations demonstrated that the I551P mutation facilitates pore opening while retaining key properties of the open WT pore.

To study the functional properties of the mutant channel in the cellular environment, we performed patch-clamp recordings of the TMEM16A I551P mutant expressed in HEK293 cells (Fig. 4*D*). Currents generated by the I551P mutant lacked the typical activation kinetics of the WT channel (Fig. 4*D*) and featured only loose coupling to voltage (*SI Appendix*, Fig. S5*A*). As a result, the mutant demonstrated almost Ohmic voltage dependence, in contrast to clear current rectification in the WT channel (Fig. 4*E*). While preserving Ca^{2+} dependence, the I551P mutant has a substantial level of activity (~37%) in the absence of Ca^{2+} (*SI Appendix*, Fig. S5*B*), indicating a constantly open pore. Application of the CaCCinh-A01 TMEM16A blocker (42) blocked a similar fraction of the current in cells expressing the mutant or WT construct (Fig. 4 *F* and *G*). As CaCCinh-A01 inhibits TMEM16A by binding to the extracellular mouth of the pore (43), these data suggest that the mutant pore retains the structural and biophysical properties of the WT pore, in agreement with our MD simulations. The WT and I551P constructs demonstrated notably different levels of protein expression, as observed in fluorescence imaging (Fig. 4*H*) and immunoblotting (*SI Appendix*, Fig. S6). To quantify the difference in the membrane-surface expression between the constructs, we calculated their linear fluorescence density along the cellular membrane (Fig. 4*I*). Assuming a uniform distribution of the channels over the membrane, we normalized the current density at +100 mV by membrane fluorescence density (Fig. 4*J*). The resulting quantity reports the current produced by a fixed number of channels (see *Materials and Methods* for details), thus allowing for a direct comparison between the constructs despite their different expression levels. The normalized current density was higher in the I551P channel than in the WT channel (Fig. 4*J*), providing further support for a higher propensity for the open-channel conformation in the mutant. Taken together, our computational and experimental results demonstrate that the I551P mutation promotes the open state of the channel by stabilizing the pi helix in TM4 and, thus, corroborate a pi-helical mechanism of pore opening in TMEM16A.

Deletion Scan Highlights the Structural and Functional Importance of the Pi-Helical Region. In protein evolution, pi helices often arise from alpha helices via a single-residue insertion (44). We, therefore, hypothesized that reversing this process via a single-residue deletion in functionally important regions could impact the TMEM16A structure. To test this hypothesis, we employed AlphaFold2 (45) (AF2) to perform a single-residue deletion scan across TM4. As shown in Fig. 5*A*, structural effects

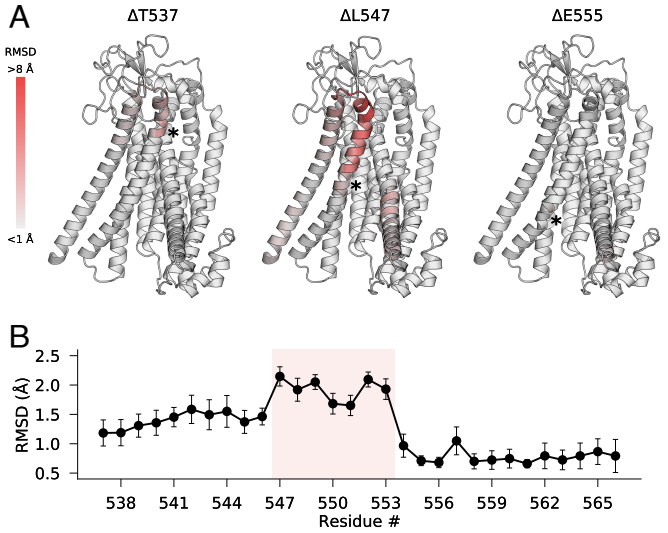

Fig. 5. AlphaFold2 deletion scanning of TM4 in TMEM16A. (*A*) Structures of ΔT537, ΔL547, and ΔE555 TMEM16A, as predicted with AlphaFold2 (AF). Residues are colored according to the RMSD from the WT structure. Asterisks indicate the positions of deletions. The intracellular parts of the protein are omitted for clarity. (*B*) Dependence of the pore RMSD on the position of the deletion in TM4. The RMSD was calculated with respect to the AF-predicted WT structures. The residue range corresponding to the central part of TM4 is highlighted. Error bars indicate the SEM, as calculated from five AF predictions.

of the deletions were mainly confined to TM3 and TM4, with the remainder of the protein largely indistinguishable from the WT prediction. Furthermore, different degrees of structural distortion were induced depending on the position of the deleted residue (Fig. 5*A*). To quantify the distortion, we calculated the RMSD of pore Cα atoms between deletion mutants and the WT structure (Fig. 5*B*). Strikingly, deletions in the central L547–L553 region of TM4 caused a prominent distortion of the TMEM16A pore, thus emphasizing the structural importance of the region. In particular, deletion of L547, which undergoes greatest structural rearrangement during the alpha-to-pi-helical transition, strongly distorted both TM3 and TM4 (Fig. 5*A* and *SI Appendix*, Fig. S7*A*), with the pore RMSD reaching more than 2 Å (Fig. 5*B*). The deletion led to a notable displacement of TM4 that was accompanied by a slight rotation of the helix (*SI Appendix*, Fig. S7*A*). In addition to TM3 and TM4, deletion of L547 also affected the intracellular half of TM6 (Fig. 5*A*). In contrast to the central region, deletions in the intracellular part of TM4 had a negligible effect on pore structure, with an RMSD of less than 1 Å (Fig. 5*B*). Slightly more prominent structural changes (RMSD of ~1.5 Å) were caused by deletions in the extracellular part of TM4. The different effects on pore structure of deletions in the intracellular and extracellular halves of TM4 are likely due to the tighter interactions of the extracellular half with other TMs.

We next performed deletion scanning of TM4 in other members of the TMEM16 family (*SI Appendix*, Fig. S8 *A–C*). In TMEM16B, another genuine Cl^- channel of the family, the results resembled those of TMEM16A: Deletions in the extracellular half of TM4 caused more pronounced structural changes, with those in the central region having a particularly strong effect (*SI Appendix*, Fig. S7*A*). In contrast, analysis of TMEM16F, the best established lipid scramblase in the family, demonstrated that any single-residue deletion in TM4 resulted in a notable structural change in the pore (RMSD of >1.5 Å) (*SI Appendix*, Fig. S8*B*). Notably, the AF2-predicted structure of WT TMEM16F features a semiopen groove (*SI Appendix*, Fig. S7*B*). Despite that, deletions in the extracellular half of TM4 led to significantly higher structural changes in TMEM16F (*SI Appendix*, Fig. S8*B*) compared to TMEM16A (Fig. 5*B*) and TMEM16B (*SI Appendix*, Fig. S8*A*), whose extracellular part of the pore is completely sealed, suggesting that the overall amino acid context rather than openness of the groove alone defines effect of the deletions on the predicted structures. Furthermore, deletions in the central region of TM4 in TMEM16F had a similar effect on the pore structure to those in other regions, with no particular increase in RMSD upon deletion of F518 (homolog of L547 in TMEM16A) (*SI Appendix*, Fig. S8*B*). These data are consistent with our previous simulations of TMEM16F (38), in which the TM4 did not undergo pi-helical transition and the pore remained closed to ion and lipid permeation. Finally, deletion scanning of the nhTMEM16 fungal lipid scramblase resulted in a flat, low-RMSD profile, with no particular effect of deletions in the TM4 central region (*SI Appendix*, Fig. S8*B*). The milder effect of the deletions in nhTMEM16 (RMSD of ~1 Å) is likely because TM4 and TM6 are separated in nhTMEM16 to provide a pathway for lipid translocation (*SI Appendix*, Fig. S7*C*). Although the structure predictions should be interpreted with caution, a distinguished structural role of the central region of TM4 in TMEM16 ion channels might relate to a more prominent functional role of pi helix in their functioning in contrast to lipid scramblases.

Pi-Helical Transition Is Prohibited in the Apo State. To gain further insight into the energetics of TMEM16A activation, we conducted a series of umbrella sampling (US) simulations of pore opening under various conditions (*SI Appendix*, Table S2). As a reaction coordinate, we used the O–N backbone distance between L545 and I550, because the decrease in this measure strongly correlated with pi-helical transition and, therefore, with pore opening in unbiased simulations. We first estimated the energetics of pore opening in the WT and I551P channels (Fig. 6*A* and *SI Appendix*, Fig. S9*A*). Consistent with the finding that pi-helical transition is only occasionally observed in unbiased simulations, the free energy was higher for the pi state than the alpha state of the WT pore (Fig. 6*B*). Introduction of the I551P mutation drastically decreased the free-energy difference between the pi and alpha states, making the former energetically more favorable (Fig. 6*B*). Thus, US simulations demonstrated that the balance between the alpha and pi states is inverted in the I551P mutant, corroborating the results of the unbiased simulations and patch-clamp experiments. Finally, to place our findings on TMEM16A opening into the more general context of channel activation, we investigated the energetics of pore opening in the apo state of TMEM16A. To this end, we conducted US simulations of the apo structure (15) (PDBID: 5OYG) resolved in Ca^{2+}-free conditions (Fig. 6*C*). Formation of the pi helix in the central part of TM4 was associated with a drastically higher change in the free energy in the apo state than in the Ca^{2+}-bound state (Fig. 6*B*). Thus, pi-helical transition is strongly disfavored in the apo state, preventing channel opening in the absence of Ca^{2+}.

To better understand the mechanism behind the increase in the free energy, we scrutinized the structures of TMEM16A in the apo and Ca^{2+}-bound states. In the apo structure, TM6 is bent around a G644 hinge toward TM4 so that the intracellular part of TM6 comes into direct contact with the central part of TM4 (Fig. 6*D*). As a result, two bulky hydrophobic residues (I648 and L652) clash with residues L547 and V548 when TM4 is in the pi-helical conformation (Fig. 6*D*). Due to this steric

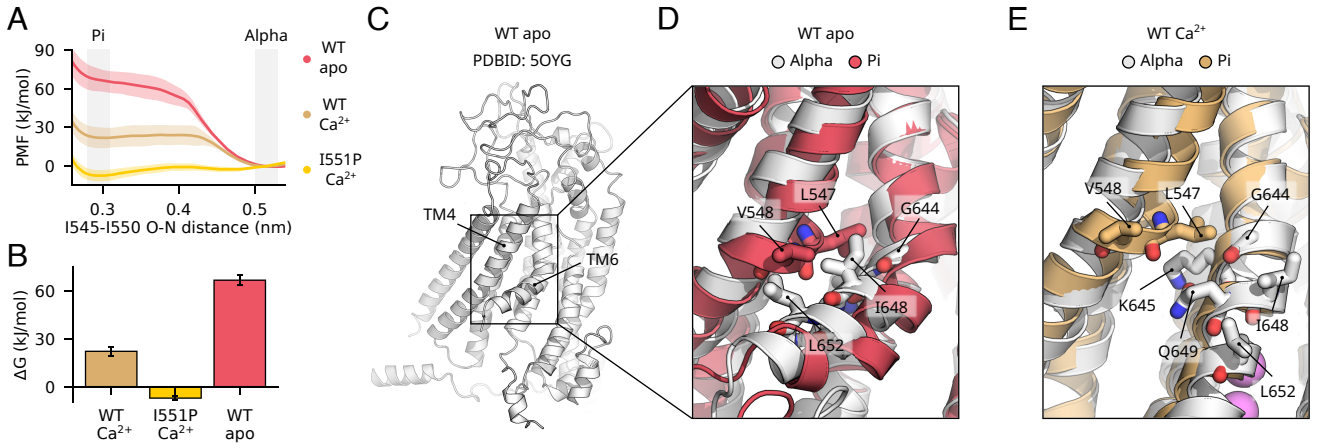

Fig. 6. Steric hindrance strongly disfavors formation of the pi helix in the apo state. (*A*) Free-energy profiles in form of the potential of mean force (PMF) of the alpha-to-pi transition in Ca^{2+}-bound and apo WT and Ca^{2+}-bound I551P TMEM16A. The O–N backbone distance between L545 and I550 was used as a reaction coordinate. Values of the reaction coordinate corresponding to the alpha and pi states are indicated in gray. (*B*) Free-energy difference (ΔG) between the alpha and pi states of the pore under different conditions. (*A* and *B*) Shaded areas and error bars indicate the SEM, as calculated from 10 US simulations. (*C*) Structure of TMEM16A in the apo state, showing a side view of the TMEM16A protomer with the intracellular N-terminus omitted for clarity. (*D* and *E*) Expanded view of the central part of the pore in the apo (*D*) and Ca^{2+}-bound (*E*) states. The pore in the alpha state (white) is aligned with the pore in the pi state (red and tan for the apo and Ca^{2+}-bound states, respectively). Key residues are shown as sticks and labeled.

clash, formation of the pi helix in the apo state leads to notable deformation of the intracellular half of TM6, with L652 displaced most prominently (Fig. 6*D*). Concordantly, the I551P mutation strongly disturbs TM6 in the apo-state simulations (*SI Appendix*, Fig. S10). Thus, L652 seems to play a profound role in hindering formation of the pi helix, providing a mechanistic explanation for the experimental observations that mutation of the bulky L652 to a smaller alanine facilitates TMEM16A activation (20, 34). In contrast, both L652 and I648 become separated from TM4 when TM6 becomes straightened in the Ca^{2+}-bound state (Fig. 6*E*). Their displacement, as well as the ample space between K645 and G644, enable free rotation of L547 that accompanies the pi-helical transition and unblocks the Cl^- conducting pore. Thus, pi-helical transition in TM4 provides a mechanistic link between the conformational changes directly induced by Ca^{2+} binding and the eventual opening of the pore in TMEM16A (Fig. 7).

Discussion

Based on our results, we propose a scheme that covers key steps of TMEM16A activation including opening of the ion-conducting pore (Fig. 7). In the apo state, the pore stays closed because the bent TM6 hinders formation of the pi helix in TM4 and the vacant Ca^{2+}-binding site creates the negative electrostatic potential that further disfavors the presence of Cl^- in the pore. In addition to the release of the electrostatic gate (40), Ca^{2+} binding straightens TM6 and primes the channel for opening by releasing the restriction on the central part of TM4. Finally, TM4 undergoes a pi-helical transition that opens a hydrated Cl^--conductive pore. More specifically, L547 loses its H-bond with I551 and bulges out of the pore, thereby unplugging the ion permeation pathway (Fig. 1). This transition is accompanied by rotation of N546 that replaces L547 inside the pore and further increases pore hydration, thus permitting the permeation of partially hydrated Cl^- ions with ~1 pS conductance (Fig. 2). Interestingly, whereas the pi-helical switch in TM4 controls permeability of the narrowest part of the TMEM16A pore, a very similar role as permeability modulator is played by a central lipid headgroup lining a proteolipidic pore in TMEM16 lipid scramblases (38). Thus, ion channels and lipid scramblases of the TMEM16 family employ different but related mechanisms to control ion permeability depending on their main physiological function.

Uncovering the mechanism of channel opening has allowed us to reveal atomistic details of the ion-conduction process in

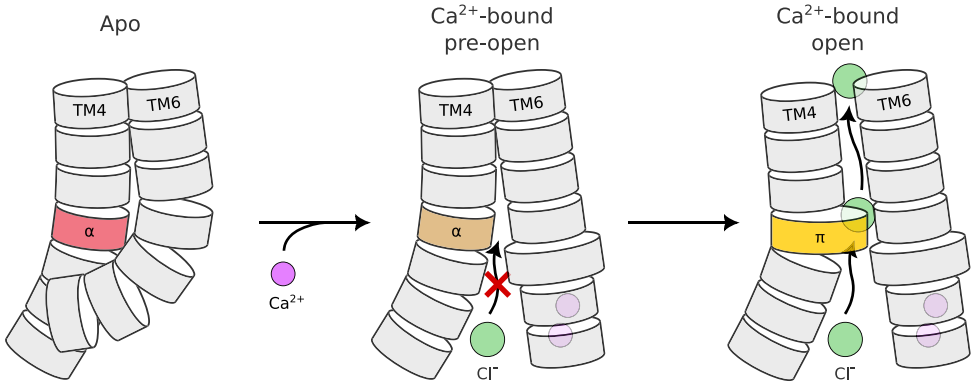

Fig. 7. Mechanism of TMEM16A activation via pi-helical transition. Schematic showing the gating mechanism in the Ca^{2+}-activated Cl^- channel TMEM16A. Wide segments represent the pi-helical (π) sections of TM4 and TM6 in contrast to narrower segments representing alpha-helical (α) sections.

TMEM16A (Fig. 3). Sufficient hydration of the pore allows ions to stay largely hydrated upon transition between two well-defined localization sites separated by the neck region. The sites are formed by a set of basic residues that create a positive electrostatic potential inside the pore, consistent with their role in anion selectivity of TMEM16A (39). Importantly, the pi-helical transition allows TMEM16A to open a Cl^--conductive pore without exposing its neck region to the membrane interior, in contrast to the proteolipidic pore of lipid scramblases (38, 46). Shielded from the membrane, the neck region has a positive electrostatic potential that guarantees stable anion selectivity for the TMEM16A pore; this contrasts with the highly variable ion selectivity of TMEM16 lipid scramblases that depends on the membrane lipid composition (38). Furthermore, this organization efficiently governs Cl^- permeation by focusing the transmembrane electric field in the neck region of the pore. The resulting voltage drop would directly affect drugs that bind to the extracellular mouth of the pore such as N-(5-nitro-1,3-thiazol-2-yl)-2-thiophenecarboxamide (NTTP), anthracene-9-carboxylic acid (A9C), and 1PBC, in full agreement with their voltage-dependent inhibition (35, 39, 47).

We found that the energetics of pi-helical transition in TM4 and concomitant pore opening are directly influenced by the Ca^{2+}-dependent conformation of TM6 (Fig. 6). When TM6 is bent around the G644 hinge in the apo state of the channel, steric hindrance between TM4 and TM6 ensures that the transition is energetically prohibited and the pore remains closed in the absence of Ca^{2+}. Interestingly, when introduced in the apo state, the I551P mutation results in a significant disturbance of TM6 (*SI Appendix*, Fig. S10) that might eventually lead to the higher channel activity in the absence of Ca^{2+} as seen in patch-clamp experiments (*SI Appendix*, Fig. S5*B*), further highlighting the important role of I551 for the first step in the TMEM16A gating mechanism (33). As TM6 straightens by forming another pi helix around the hinge region, the overall gating mechanism can be crudely described as two consecutive pi-helical transitions. The first takes place in TM6 as a direct response to Ca^{2+} binding and this primes the channel for opening via formation of the second pi helix in TM4. Thus, our results provide a mechanism for the recently proposed coupling between pi helix formation in TM6 and opening of the inner gate of the pore (36). Our data suggest that the inner hydrophobic gate is partially formed by L547, in addition to the triad of isoleucine residues (I550, I551, and I641) that was previously proposed to gate the pore (33, 34). We further propose that I551, which lies alongside the ion permeation pathway, is coupled to TMEM16A gating in a largely indirect manner by affecting the dynamics of pi-helical transition in TM4. In particular, I551 forms a hydrogen bond with L547 such that disruption of this bond leads to formation of the pi helix and concomitant opening of the pore. Disrupting this bond by introducing the I551P mutation stabilized the pi-helical state of the pore and, thereby, facilitated activation of TMEM16A both in simulations and experiment (Fig. 4). Furthermore, a substitution of a bulky I551 with smaller alanine, which is less restricted by the surrounding residues, also promotes pi-helical formation in simulations (*SI Appendix*, Fig. S3), offering a mechanistic explanation for the experimentally observed increase in the channel activation upon reduction of the hydrophobic volume of the gating triad (34). Our results provide a mechanistic description of the crucial role that the central part of TM4 plays in the initial TM6 rearrangement and transition of the channel from the preopen to the open state, which constitute the first and the last steps of the recently proposed mechanism of TMEM16A activation (33).

Intriguingly, I551 in TMEM16A is homologous to P341 in nhTMEM16 (*SI Appendix*, Fig. S8*D*). We analyzed simulation trajectories from our previous study (38) and found that no pi helix was formed above P341, despite disturbance of the alpha-helical structure of TM4 in nhTMEM16. This finding further highlights the importance of context for the pi-helical transition, as also demonstrated by our AlphaFold2 deletion scan (Fig. 5). We speculate that disturbance of the alpha-helical structure of TM4 by a proline residue might have played a role in developing the gating mechanism during the evolution of TMEM16 channels and lipid scramblases. Interestingly, a recent study reported potentiation of both ion and lipid conduction in TMEM16 and OSCA/TMEM63 proteins upon substitution of TM4 residues with lysine, further supporting the crucial functional role of the central part of TM4 in both protein families (48). To gain further insight into the possible roles of TM4 and pi-helical transition in related channels, we scrutinized the sequences and AF2-predicted structures of a homologous family of OSCA/TMEM63 channels (49, 50). We found that all family members have a conserved proline (*SI Appendix*, Fig. S11*A*) that disturbs the helical structure of the central part of TM4 (*SI Appendix*, Fig. S11*B*) as also observed in experimental structures (50–54). Strikingly, and in contrast to other isoforms, AtOSCA4.1 has an insertion (S479) in the central part of TM4 (*SI Appendix*, Fig. S11*A*), resulting in the formation of a genuine pi helix similar to the one we observed in TMEM16A (*SI Appendix*, Fig. S11*B*). Given that insertions and deletions represent high-risk, high-reward mutations (55), these data suggest that the central region of TM4 and its pi-helix might be of general functional importance in a broad spectrum of TMEM16-related proteins.

A crucial role for dynamic pi helices in controlling ion channel gating is becoming increasingly evident in various types of ion channels (56) such as P-loop cation channels (57) that include voltage gated sodium (Nav) (58, 59) and transient receptor potential (TRP) channels (56). In particular, both activation (59) and fast inactivation (60) are modulated by a pi-helical transition in Nav channels. Importantly, the state-dependent action of certain Nav-targeting drugs has been shown to rely on reciprocal modulation between drug binding and pi-helical transition (60, 61). Our findings add another example of pi-helical gating in Ca^{2+}-activated Cl^- channels, and we believe that the identification of this gating mechanism might lead to more efficient treatments for cancer and CF via the development of state-specific drugs targeting TMEM16A.

Materials and Methods

Protein Models. The pore-open Ca^{2+}-bound (35) and closed apo (15) states of murine TMEM16A (*ac* splice variant; UniProt ID: Q8BHY3) were modeled based on the cryo-EM structures with PDB IDs 7ZK3 and 5OYG, respectively, with a final residue range of 115 to 911. The molecule of 1PBC that blocks the pore in the preopen state (35) was removed from the structure before simulations. Missing residues that were unresolved in the original structures were restored using Modeller version 9.18 (62). The disulfide bonds were imposed between the cysteine pairs C382–C386, C379–C836, C370–C395, and C625–C630, as guided by the cryo-EM structures and functional data (18). In all protein models, the N and C termini were capped with acetyl and N-methyl, respectively. The standard protonation state at neutral pH was assigned to all residues.

Simulation Parameters. The simulations were performed using GROMACS (63) version 2021, with a time step of 2 fs. A pressure of 1 bar was applied semi-isotropically with a time constant of 5 ps, using either the c-rescale (64) or the Berendsen (65) barostat. A temperature of 310 K was maintained with the v-rescale thermostat (66) using a time constant of 0.5 ps. Van der Waals interactions were described by the Lennard-Jones potential with a cutoff radius of 1.2 nm, with forces smoothly switched to zero in the range of 1.0 to 1.2 nm without a dispersion correction. Electrostatic interactions were calculated by the smooth particle mesh Ewald (SPME) method (67, 68), with a real-space cutoff distance of 1.2 nm. CHARMM36 force field parameters were used for lipids (69) and CHARMM36m force field parameters for proteins (70). All hydrogen-involving bonds were constrained with LINCS (71). Ions were described using CHARMM parameters with the NBFIX correction (72), and the CHARMM TIP3P model was used for water molecules.

Simulated Systems and Replication. The proteins were embedded in a 1-palmitoyl-2-oleoyl-phosphatidylcholine (POPC) bilayer using the *g_membed* function (73) in GROMACS. The initial protein orientation within the membrane was guided by the corresponding structure from the Orientations of Proteins in Membranes database (74). Na^+ and Cl^- were added to the solution with a bulk concentration of approximately 150 mM NaCl.

Each simulated system was replicated five times, so that the data on 10 independent protomers could be collected for each condition. To ensure independence between the replicates, we prepared them using different initial configurations of the membrane, which were taken from a simulation of a pure POPC bilayer. Each replicate was individually equilibrated in three steps for in total 71 ns. First, it was simulated for 1 ns with position restraints on Ca^{2+} ions and all heavy atoms of the protein in all dimensions and all heavy atoms of the lipids in the *z*-dimension. Second, the membrane around the protein was equilibrated for 50 ns with only protein heavy atoms and Ca^{2+} ions restrained. Finally, the side chains of the protein and Ca^{2+} ions were equilibrated for 20 ns with the restrains only on the protein backbone atoms. The restraints were applied by a harmonic potential with a force constant of 1,000 $kJ \cdot mol^{-1} \cdot nm^{-2}$. Production simulations were run for 1 to 2 μs (*SI Appendix*, Table S1). In the simulations of the I551P mutant, the mutation was introduced using the mutagenesis plugin in PyMOL (version 2.5) in the WT systems after the second equilibration step.

To bias the TMEM16A pore to the alpha or pi state, distance restraints in form of the harmonic potential with a force constant of 10,000 $kJ \cdot mol^{-1} \cdot nm^{-2}$ were applied on the O–N distance between L547 and I551 or L545 and I550, respectively. In simulations with transmembrane voltage, it was created by applying a constant electric field (75) of ±10 mV/nm along the *z*-axis of the simulation box resulting in the transmembrane voltage of around ±140 mV.

Umbrella Sampling Simulations. Initial system configurations for the umbrella windows were taken from the trajectory generated by the pull code in GROMACS. The 100-ns-long pulling was done on the equilibrated structure to induce alpha-to-pi transition along the reaction coordinate defined as the O–N backbone distance between L545 and I550. Thirty US windows were uniformly distributed along the distance range from 0.25 to 0.55 nm and simulated for 50 ns. Each window was restrained to the target value of the reaction coordinate by the harmonic potential with a force constant of 50,000 $kJ \cdot mol^{-1} \cdot nm^{-2}$, that ensured sufficient sampling in the sub-Å range (*SI Appendix*, Fig. S9*B*). The first 20 ns of the simulation accounted for the system equilibration and therefore were discarded from the analysis. The resulting free-energy profiles were calculated using the weighted histogram analysis method as implemented in *g_wham* tool in GROMACS (76). The pulling and US simulations were conducted in parallel on two protomers within the dimer, resulting in 10 free-energy profiles calculated from five independent simulations. To calculate the free-energy difference (ΔG) between the alpha and pi states of the pore, they were defined by the reaction coordinate ranging from 0.28 to 0.31 nm and from 0.50 to 0.53 nm, respectively.

Simulation Analysis. Prior to analysis, simulation trajectories were translationally and rotationally fitted onto the transmembrane region of the original protein structure and sampled every 100 ps. The distance between TM4 and TM5 was defined as the distance between Cα atoms of N546 and P595. The central part of the pore was defined as a 1-nm-long region above the center of geometry of Cα atoms of residues I551, S592, and K645. All distributions along the pore axis were centered at the Cα position of S592. Profile of the pore radius along the *z*-axis was calculated from the water occupancy map as $\sqrt{A(z)/\pi}$, where $A(z)$ is the area of the water-occupancy slab with the occupancy higher than 10%. The narrowest part of the pore was found to span 3 Å near the pore center defined by the Cα position of S592. Hydration number of a Cl^- ion was calculated as the number of water oxygen atoms within 3.8 Å of its position. A protein residue was considered in contact with a permeating Cl^- ion if any of its heavy atoms was within 5 Å of the ion position. In unbiased simulations, the pore was assigned to the pi state if the O–N distance between L545 and I550 was below 3.6 Å. Ion conductance was calculated as the number of observed permeation events divided by the applied transmembrane voltage and total simulation time. CI was estimated by bootstrapping conductance of individual protomers with 9,999 resamples. All analyses were done with GROMACS tools and bespoke python scripts using the MDAnalysis library (77).

Electrostatics and voltage coupling was quantified with *g_elpot* that employs the SPME method together with explicit water molecules to extract convergent distribution of electrostatic potential of high resolution from atomistic MD simulations (41). We used β of 20 nm^{-1} and a grid size of 360 × 360 × 280 (resulting in a grid spacing of ∼0.5 Å) for calculating the electrostatic potential. No rotational fitting was done on the input trajectory prior to the calculations as required by the tool, whereas high resolution of the final map was achieved by the on-the-fly fitting of the protein transmembrane region onto the reference structure. The electrostatic-potential profiles were calculated by combining the electrostatic-potential and water-occupancy maps, as previously described (41, 78). In case of the electric-field application, the profiles were corrected by the potential created by the field (78). The voltage-fraction profiles were calculated by subtracting the electrostatic-potential profiles upon electric-field application from those at zero voltage and dividing the result by the value of the transmembrane voltage (78).

Sequence alignment was done using the ClustalW program (79). All visualizations were done using PyMOL version 2.5.

Structure Predictions by AlphaFold2. The deletion scan was done by structure predictions performed with AlphaFold2 version 2.3.1 (45). Five predictions per sequence were done with the monomer model preset, and the maximum template release date was set to 2017-04-30. To avoid structural inference by disordered regions of a protein, we trimmed the N- and C-terminal parts of the sequences. The resulting sequences covered residues 58–927 (TMEM16A; UniProt ID: Q8BHY3), 95–960 (TMEM16B; UniProt ID: Q8CFW1), 67–898 (TMEM16F; UniProt ID: Q6P9J9), and 17–650 (nhTMEM16; UniProt ID: C7Z7K1). Structures of OSCA channels were taken from the AlphaFold2 database (80).

Cell Line and Plasmids. HEK293 cultures (DSMZ, No. ACC-305) were maintained in humidified incubators at 37 °C and 95% air/5% CO_2 in Dulbecco's modified Eagle Medium (DMEM, PAN-Biotech), supplemented with 10% FBS, 1% penicillin/streptomycin, and 1% glutamine. The *ac* splice variant of mouse TMEM16A (UniProt ID: Q8BHY3) fused with eGFP was subcloned into a pcDNA3.1 vector. Mutant I551P construct was generated using PCR-based mutagenesis and verified by DNA sequencing.

Patch-Clamp Electrophysiology and Fluorescence Measurements. HEK293 cells were transiently transfected using the calcium phosphate coprecipitation method and were used within 24 to 36 h after transfection. Patch pipettes were pulled from borosilicate glass capillaries (O.D. 1.5 mm, I.D. 0.86 mm, Harvard Apparatus) and were fire-polished with a microforge (Narishige), with the final pipette resistance of 3 to 5 mΩ. Currents were recorded with an EPC-10 USB patch-clamp amplifier and PatchMaster software (HEKA Elektronik). Currents were low-pass filtered at 10 kHz and sampled at 50 kHz. The holding potential was set to −30 mV, and the standard voltage-step protocol consisted of a 100-ms prepulse to −80 mV followed

by steps from −100 mV to 100 mV with the 20-mV increment. Bath solution contained 140 mM NaCl, 2 mM $MgCl_2$, 4 mM $CaCl_2$, 5 mM TEA-Cl, and 10 mM HEPES at pH 7.4 adjusted by NMDG. Solution with CaCCinh-A01 (Tocris) was prepared by adding the blocker dissolved in DMSO to the stock bath solution to reach 20 μM concentration. The blocker was applied by solution exchange via a manual perfusion system. Pipette solution with ∼250 nM free Ca^{2+}, as calculated by MAXCHELATOR (https://somapp.ucdmc.ucdavis.edu/pharmacology/bers/maxchelator), contained 140 mM NaCl, 2 mM $MgCl_2$, 5 mM EGTA, 3.79 mM $Ca(OH)_2$, and 10 mM HEPES at pH 7.4 adjusted by NMDG. In the dose-response experiments, Ca^{2+}-free and 1 mM-Ca^{2+} stock solutions were mixed to reach a desired concentration of free Ca^{2+}. The Ca^{2+}-free solution contained 140 mM NaCl, 2 mM $MgCl_2$, 5 mM EGTA, and 10 mM HEPES at pH 7.4. The 1 mM-Ca^{2+} solution contained 140 mM NaCl, 2 mM $MgCl_2$, 5 mM EGTA, 6 mM $Ca(OH)_2$, and 10 mM HEPES at pH 7.4. All experiments were performed at 20 to 22 °C. The dose–response data were fitted with the Hill equation

$$I/I_{max} = f_0 + \frac{1 - f_0}{1 + \left(\frac{EC_{50}}{[Ca^{2+}]}\right)^h}, \quad [1]$$

where EC_{50} is concentration of half-maximum activation, h is the Hill coefficient, and f_0 is approximated fraction of maximum current at zero $[Ca^{2+}]$.

Fluorescence measurements were conducted on a Leica DMi8 THUNDER (Leica) using an HC PL APO 63×/1.4 oil immersive objective, with eGFP fluorescence excited at 475 nm and detected at 535 nm. The membrane region was manually selected with the segmented-line selection tool in ImageJ (81) (version 1.54g) using a line width of 1.023 μm (10 pixels). Membrane fluorescence density was calculated as the total fluorescence of the selected membrane region divided by its length. Given a finite depth of field, this quantity reports on the fluorescence of a membrane surface element that is proportional to the number of channels in this surface element. Thus, current density normalized by the fluorescence density is proportional to the current produced by a single channel. Importantly, the coefficient of proportionality remains invariant over different channel constructs, assuming that mutations do not change fluorescence yield of a single channel. As a result, by the fluorescence normalization of the whole-cell current density we can directly compare the level of the mean single-channel current between constructs which exhibit different levels of surface expression.

Immunoblotting. Cells were collected by scraping on ice in precooled RIPA buffer (150 mM NaCl, 50 mM Tris, pH 8.0, 5 mM EDTA, pH 8.0, 1% NP-40, 0.5% sodium deoxycholate, 0.1% SDS) containing proteinase inhibitor cocktail (Roche, Basel, Switzerland). The suspension was incubated on ice for 30 min and vortexed every 10 min. After subsequent centrifugation at 16,000×g at 4 °C for 20 min, the supernatant was mixed with SDS sample buffer. Cell lysates were separated by 10% SDS-PAGE and transferred to nitrocellulose membranes (Macherey-Nagel, Düren, Germany) at 400 mA for 90 min. After the transfer, the membranes were blocked with 5%-bovine serum albumin in Tris-buffered saline-Tween 20 (TBS-T) solution, containing 20 mm Tris, pH 7.6, 150 mM NaCl, and 0.02% Tween-20 for 1 h at room temperature, and subsequently incubated with primary antibodies overnight at 4 °C. Primary antibodies and dilutions used: anti-GFP (DSHB; DSHB-GFP-1D2; RRID:AB_2617419) 1:1,000; anti-GAPDH (Abcam; Catalog No. ab9485; RRID:AB_307275): dilution 1:5,000. After three washes for 10 min each with TBS-T, the membranes were incubated with donkey anti-mouse IgG secondary antibody (Abcam; catalog. no. ab205724; RRID:AB_2904602), dilution 1:10,000 for 1 h at room temperature, washed with TBS-T, and finally developed with enhanced chemiluminescence reagent (SuperSignal kit; Thermo Fisher Scientific) on a digital imaging system (Azure Biosystems, Dublin, CA; #1.6.4.1229). Protein levels were quantified using ImageJ (81) (version 1.54g).

Data, Materials, and Software Availability. Some study data are available: Simulation data are archived at Jülich Supercomputing Centre and are available from the corresponding author upon reasonable request.

ACKNOWLEDGMENTS. We thank Anna Klemmer and Fan Wang for excellent technical assistance and Dr. Claudia Alleva for helpful discussions. This work was funded by the Deutsche Forschungsgemeinschaft (German Research Foundation)–426950122 (MA 7525/1-2, as part of the Research Unit FOR 2518, DynIon, project P4; and MA 7525/2-2, as part of the Research Unit FOR 5046, project P2). We gratefully acknowledge the computing time granted through JARA on the supercomputer JURECA at Forschungszentrum Jülich under Grant No. ano1.

Author affiliations: [a]Institute of Biological Information Processing (IBI-1), Molekular- und Zellphysiologie, Forschungszentrum Jülich, Jülich 52428, Germany; [b]Institute for Molecular Medicine, MSH Medical School Hamburg, Hamburg 20457, Germany; and [c]Institute of Neurophysiology, Hannover Medical School, Hannover 30625, Germany

1. A. Caputo *et al.*, *TMEM16A: A Membrane Protein Associated with Calcium-Dependent Chloride Channel Activity* (Science, New York, NY, 2008), vol. 322, pp. 590–594.
2. B. C. Schroeder, T. Cheng, Y. N. Jan, L. Y. Jan, Expression cloning of TMEM16A as a calcium-activated chloride channel subunit. *Cell* **134**, 1019–1029 (2008).
3. Y. D. Yang *et al.*, TMEM16A confers receptor-activated calcium-dependent chloride conductance. *Nature* **455**, 1210–1215 (2008).
4. N. Pedemonte, L. J. V. Galietta, Structure and function of TMEM16 proteins (anoctamins). *Physiol. Rev.* **94**, 419–459 (2014).
5. Q. Ji *et al.*, Recent advances in TMEM16A: Structure, function, and disease. *J. Cell. Physiol.* **234**, 7856–7873 (2018).
6. C. Mitri, H. Sharma, H. Corvol, O. Tabary, TMEM16A/Ano1: Current strategies and novel drug approaches for cystic fibrosis. *Cells* **10**, 2867 (2021).
7. D. Crottès, L. Y. Jan, The multifaceted role of TMEM16A in cancer. *Cell Calcium* **82**, 102050 (2019).
8. R. Al-Hosni, Z. Ilkan, E. Agostinelli, P. Tammaro, The pharmacology of the TMEM16A channel: Therapeutic opportunities. *Trends Pharmacol. Sci.* **43**, 712–725 (2022).
9. G. Fallah *et al.*, TMEM16A(a)/anoctamin-1 shares a homodimeric architecture with ClC chloride channels. *Mol. Cell. Proteomics* **10**, M110.004697 (2011).
10. J. T. Sheridan *et al.*, Characterization of the oligomeric structure of the Ca^{2+}-activated Cl^- channel Ano1/TMEM16A. *J. Biol. Chem.* **286**, 1381–1388 (2011).
11. J. Tien, H. Y. Lee, D. L. Minor, Y. N. Jan, L. Y. Jan, Identification of a dimerization domain in the TMEM16A calcium-activated chloride channel (CaCC). *Proc. Natl. Acad. Sci. U.S.A.* **110**, 6352–6357 (2013).
12. N. K. Lim, A. K. Lam, R. Dutzler, Independent activation of ion conduction pores in the double-barreled calcium-activated chloride channel TMEM16A. *J. Gen. Physiol.* **148**, 375–392 (2016).
13. G. Jeng, M. Aggarwal, W. P. Yu, T. Y. Chen, Independent activation of distinct pores in dimeric TMEM16A channels. *J. Gen. Physiol.* **148**, 393–404 (2016).
14. C. Paulino *et al.*, Structural basis for anion conduction in the calcium-activated chloride channel TMEM16A. *eLife* **6**, e26232 (2017).
15. C. Paulino, V. Kalienkova, A. K. M. Lam, Y. Neldner, R. Dutzler, Activation mechanism of the calcium-activated chloride channel TMEM16A revealed by cryo-EM. *Nature* **552**, 421–425 (2017).
16. S. Dang *et al.*, Cryo-EM structures of the TMEM16A calcium-activated chloride channel. *Nature* **552**, 426–429 (2017).
17. J. D. Brunner, N. K. Lim, S. Schenck, A. Duerst, R. Dutzler, X-ray structure of a calcium-activated TMEM16 lipid scramblase. *Nature* **516**, 207–212 (2014).
18. K. Yu, C. Duran, Z. Qu, Y. Y. Cui, H. C. Hartzell, Explaining calcium-dependent gating of anoctamin-1 chloride channels requires a revised topology. *Circ. Res.* **110**, 990–999 (2012).
19. J. Tien *et al.*, A comprehensive search for calcium binding sites critical for TMEM16A calcium-activated chloride channel activity. *eLife* **3**, e02772 (2014).
20. C. J. Peters *et al.*, The sixth transmembrane segment is a major gating component of the TMEM16A calcium-activated chloride channel. *Neuron* **97**, 1063–1077.e4 (2018).
21. S. C. Le, H. Yang, An additional Ca^{2+} binding site allosterically controls TMEM16A activation. *Cell Rep.* **33**, 108570 (2020).
22. Q. Xiao *et al.*, Voltage- and calcium-dependent gating of TMEM16A/Ano1 chloride channels are physically coupled by the first intracellular loop. *Proc. Natl. Acad. Sci. U.S.A.* **108**, 8891–8896 (2011).
23. S. Cruz-Rangel *et al.*, Extracellular protons enable activation of the calcium-dependent chloride channel TMEM16A. *J. Physiol.* **595**, 1515–1531 (2017).
24. J. J. De Jesús-Pérez *et al.*, Gating and anion selectivity are reciprocally regulated in TMEM16A (Ano1). *J. Gen. Physiol.* **154**, e202113027 (2022).
25. J. J. De Jesés-Pérez *et al.*, Phosphatidylinositol 4,5-bisphosphate, cholesterol, and fatty acids modulate the calcium-activated chloride channel TMEM16A (Ano1). *Biochim. Biophys. Acta (BBA): Mol. Cell Biol. Lipids* **1863**, 299–312 (2018).
26. C. M. Ta, K. E. Acheson, N. J. G. Rorsman, R. C. Jongkind, P. Tammaro, Contrasting effects of phosphatidylinositol 4,5-bisphosphate on cloned TMEM16A and TMEM16B channels. *Br. J. Pharmacol.* **174**, 2984–2999 (2017).
27. K. Yu, T. Jiang, Y. Cui, E. Tajkhorshid, H. C. Hartzell, A network of phosphatidylinositol 4,5-bisphosphate binding sites regulates gating of the Ca^{2+}-activated Cl^- channel Ano1 (TMEM16A). *Proc. Natl. Acad. Sci. U.S.A.* **116**, 19952–19962 (2019).
28. M. Tembo, K. L. Wozniak, R. E. Bainbridge, A. E. Carlson, Phosphatidylinositol 4,5-bisphosphate (PIP_2) and Ca^{2+} are both required to open the Cl^- channel TMEM16A *J. Biol. Chem.* **294**, 12556–12564 (2019).
29. J. Arreola, H. C. Hartzell, Wasted TMEM16A channels are rescued by phosphatidylinositol 4,5-bisphosphate. *Cell Calcium* **84**, 102103 (2019).
30. S. C. Le, Z. Jia, J. Chen, H. Yang, Molecular basis of PIP_2-dependent regulation of the Ca^{2+}-activated chloride channel TMEM16A. *Nat. Commun.* **10**, 3769 (2019).
31. Z. Jia, J. Chen, Specific PIP_2 binding promotes calcium activation of TMEM16A chloride channels. *Commun. Biol.* **4**, 259 (2021).

32. J. A. Contreras-Vite *et al*., Revealing the activation pathway for TMEM16A chloride channels from macroscopic currents and kinetic models. *Pflügers Arch.: Eur. J. Physiol.* **468**, 1241–1257 (2016).
33. A. K. M. Lam, R. Dutzler, Mechanism of pore opening in the calcium-activated chloride channel TMEM16A. *Nat. Commun.* **12**, 786 (2021).
34. A. K. M. Lam, J. Rheinberger, C. Paulino, R. Dutzler, Gating the pore of the calcium-activated chloride channel TMEM16A. *Nat. Commun.* **12**, 785 (2021).
35. A. K. M. Lam, S. Rutz, R. Dutzler, Inhibition mechanism of the chloride channel TMEM16A by the pore blocker 1PBC. *Nat. Commun.* **13**, 2798 (2022).
36. A. K. M. Lam, R. Dutzler, Mechanistic basis of ligand efficacy in the calcium-activated chloride channel TMEM16A. *EMBO J.* **42**, e115030 (2023).
37. B. Manoury, A. Tamuleviciute, P. Tammaro, TMEM16A/anoctamin 1 protein mediates calcium-activated chloride currents in pulmonary arterial smooth muscle cells. *J. Physiol.* **588**, 2305–2314 (2010).
38. A. Y. Kostritskii, J. P. Machtens, Molecular mechanisms of ion conduction and ion selectivity in TMEM16 lipid scramblases. *Nat. Commun.* **12**, 2826 (2021).
39. C. J. Peters *et al*., Four basic residues critical for the ion selectivity and pore blocker sensitivity of TMEM16A calcium-activated chloride channels. *Proc. Natl. Acad. Sci. U.S.A.* **112**, 3547–3552 (2015).
40. A. K. Lam, R. Dutzler, Calcium-dependent electrostatic control of anion access to the pore of the calcium-activated chloride channel TMEM16A. *eLife* **7**, e39122 (2018).
41. A. Y. Kostritskii, C. Alleva, S. Cönen, J. P. Machtens, g_elpot: A tool for quantifying biomolecular electrostatics from molecular dynamics trajectories. *J. Chem. Theory Comput.* **17**, 3157–3167 (2021).
42. E. Bradley *et al*., Pharmacological characterization of TMEM16A currents. *Channels (Austin, Tex.)* **8**, 308–320 (2014).
43. S. Shi *et al*., Molecular mechanism of $CaCC_{inh}$-A01 inhibiting TMEM16A channel. *Arch. Biochem. Biophys.* **695**, 108650 (2020).
44. R. B. Cooley, D. J. Arp, P. A. Karplus, Evolutionary origin of a secondary structure: π-helices as cryptic but widespread insertional variations of α-helices that enhance protein functionality. *J Mol Biol* **404**, 232–246 (2010).
45. J. Jumper *et al*., Highly accurate protein structure prediction with alphafold. *Nature* **596**, 583–589 (2021).
46. T. Jiang, K. Yu, H. C. Hartzell, E. Tajkhorshid, Lipids and ions traverse the membrane by the same physical pathway in the nhTMEM16 scramblase. *eLife* **6**, e28671 (2017).
47. R. L. Dinsdale *et al*., An outer-pore gate modulates the pharmacology of the TMEM16A channel. *Proc. Natl. Acad. Sci. U.S.A.* **118**, e2023572118 (2021).
48. A. J. Lowry *et al*., TMEM16 and OSCA/TMEM63 proteins share a conserved potential to permeate ions and phospholipids. *eLife* **13**, RP96957 (2024).
49. S. E. Murthy *et al*., OSCA/TMEM63 are an evolutionarily conserved family of mechanically activated ion channels. *eLife* **7**, e41844 (2018).
50. M. Zhang *et al*., Structure of the mechanosensitive OSCA channels. *Nat. Struct. Mol. Biol.* **25**, 850–858 (2018).
51. X. Liu, J. Wang, L. Sun, Structure of the hyperosmolality-gated calcium-permeable channel OSCA1.2. *Nat. Commun.* **9**, 5060 (2018).
52. S. Jojoa-Cruz *et al*., Cryo-EM structure of the mechanically activated ion channel OSCA1.2. *eLife* **7**, e41845 (2018).
53. K. Maity *et al*., Cryo-EM structure of OSCA1.2 from *Oryza sativa* elucidates the mechanical basis of potential membrane hyperosmolality gating. *Proc. Natl. Acad. Sci. U.S.A.* **116**, 14309–14318 (2019).
54. S. Jojoa-Cruz, B. Burendei, W. H. Lee, A. B. Ward, Structure of mechanically activated ion channel OSCA2.3 reveals mobile elements in the transmembrane domain. *Structure* **32**, 157–167.e5 (2024).
55. S. Savino, T. Desmet, J. Franceus, Insertions and deletions in protein evolution and engineering. *Biotechnol. Adv.* **60**, 108010 (2022).
56. L. Zubcevic, S. Y. Lee, The role of π-helices in TRP channel gating. *Curr. Opin. Struct. Biol.* **58**, 314–323 (2019).
57. D. B. Tikhonov, B. S. Zhorov, Conservation and variability of the pore-lining helices in p-loop channels. *Channels* **11**, 660–672 (2017).
58. G. Huang *et al*., High-resolution structures of human Nav1.7 reveal gating modulation through *alpha-pi* helical transition of $S6_{IV}$. *Cell Rep.* **39**, 110735 (2022).
59. K. Choudhury, L. Delemotte, Modulation of pore opening of eukaryotic sodium channels by π-helices in S6. *J. Phys. Chem. Lett.* **14**, 5876–5881 (2023).
60. J. Zhang *et al*., Structural basis for Nav1.7 inhibition by pore blockers. *Nat. Struct. Mol. Biol.* **29**, 1208–1216 (2022).
61. M. Lenaeus, T. M. Gamal El-Din, L. Tonggu, N. Zheng, W. A. Catterall, Structural basis for inhibition of the cardiac sodium channel by the atypical antiarrhythmic drug ranolazine. *Nat. Cardiovasc. Res.* **2**, 587–594 (2023).
62. A. Šali, T. L. Blundell, Comparative protein modelling by satisfaction of spatial restraints. *J. Mol. Biol.* **234**, 779–815 (1993).
63. M. J. Abraham *et al*., GROMACS: High performance molecular simulations through multi-level parallelism from laptops to supercomputers. *SoftwareX* **1–2**, 19–25 (2015).
64. M. Bernetti, G. Bussi, Pressure control using stochastic cell rescaling. *J. Chem. Phys.* **153**, 114107 (2020).
65. H. J. C. Berendsen, J. P. M. Postma, W. F. van Gunsteren, A. DiNola, J. R. Haak, Molecular dynamics with coupling to an external bath. *J. Chem. Phys.* **81**, 3684–3690 (1984).
66. G. Bussi, D. Donadio, M. Parrinello, Canonical sampling through velocity rescaling. *J. Chem. Phys.* **126**, 014101 (2007).
67. U. Essmann *et al*., A smooth particle mesh Ewald method. *J. Chem. Phys.* **103**, 8577–8593 (1995).
68. T. Darden, D. York, L. Pedersen, Particle mesh Ewald: An n·log(n) method for Ewald sums in large systems. *J. Chem. Phys.* **98**, 10089–10092 (1993).
69. J. B. Klauda *et al*., Update of the CHARMM all-atom additive force field for lipids: Validation on six lipid types. *J. Phys. Chem. B* **114**, 7830–7843 (2010).
70. J. Huang *et al*., CHARMM36m: An improved force field for folded and intrinsically disordered proteins. *Nat. Methods* **14**, 71–73 (2017).
71. B. Hess, H. Bekker, H. J. Berendsen, J. G. Fraaije, LINCS: A linear constraint solver for molecular simulations. *J. Comput. Chem.* **18**, 1463–1472 (1997).
72. J. Yoo, A. Aksimentiev, Improved parametrization of Li^+, Na^+, K^+, and Mg^{2+} ions for all-atom molecular dynamics simulations of nucleic acid systems *J. Phys. Chem. Lett.* **3**, 45–50 (2012).
73. M. G. Wolf, M. Hoefling, C. Aponte-Santamaría, H. Grubmüller, G. Groenhof, g_membed: Efficient insertion of a membrane protein into an equilibrated lipid bilayer with minimal perturbation. *J. Comput. Chem.* **31**, 2169–2174 (2010).
74. M. A. Lomize, I. D. Pogozheva, H. Joo, H. I. Mosberg, A. L. Lomize, OPM database and ppm web server: Resources for positioning of proteins in membranes. *Nucleic Acids Res.* **40**, D370–D376 (2012).
75. B. Roux, The membrane potential and its representation by a constant electric field in computer simulations. *Biophys. J.* **95**, 4205–4216 (2008).
76. J. S. Hub, B. L. de Groot, D. van der Spoel, g_wham–A free weighted histogram analysis implementation including robust error and autocorrelation estimates. *J. Chem. Theory Comput.* **6**, 3713–3720 (2010).
77. N. Michaud-Agrawal, E. J. Denning, T. B. Woolf, O. Beckstein, MDAnalysis: A toolkit for the analysis of molecular dynamics simulations. *J. Comput. Chem.* **32**, 2319–2327 (2011).
78. A. Y. Kostritskii, J. P. Machtens, Domain- and state-specific shape of the electric field tunes voltage sensing in voltage-gated sodium channels. *Biophys. J.* **122**, 1807–1821 (2023).
79. J. D. Thompson, D. G. Higgins, T. J. Gibson, CLUSTAL W: Improving the sensitivity of progressive multiple sequence alignment through sequence weighting, position-specific gap penalties and weight matrix choice. *Nucleic Acids Res.* **22**, 4673–4680 (1994).
80. M. Varadi *et al*., Alphafold protein structure database: Massively expanding the structural coverage of protein-sequence space with high-accuracy models. *Nucleic Acids Res.* **50**, D439–D444 (2021).
81. C. A. Schneider, W. S. Rasband, K. W. Eliceiri, NIH Image to ImageJ: 25 years of image analysis. *Nat. Methods* **9**, 671–675 (2012).